Interfacial Water Flipping and Electrostatic Fields at the Electrode:Electrolyte Interface from *operando* Nonlinear Optical Spectroscopy

Raiden Speelman and Franz M. Geiger*

Department of Chemistry, Northwestern University,

2145 Sheridan Road, Evanston, IL 60660, USA

*f-geiger@northwestern.edu

Abstract. Water's oxygen is the electron source in the industrially important oxygen evolution reaction, but how water interacts with an electrode's active sites remains poorly understood. Much microscopic insight into the Stern layer water structure and the interfacial fields currently comes from atomistic simulations,[1-6] with joint theoretical and surface-specific experimental studies just emerging.[7-9] The strong absorber problem for water in particular has hampered our molecular understanding of how the water molecules in the Stern layer orient themselves in response to an externally applied potential. Here, we employ *operando* nonlinear optics with a non-resonant pulse triplet while recording cyclic voltammograms at Ni:NiOx electrodes in contact with pH 13 electrolyte. We quantify the number of net-aligned Stern layer water molecules that point their oxygen atoms towards the electrode in response to the externally applied potential and obtain the total electrostatic field across the electrical double layer by quantifying the total potential. We find that the energy associated with water flipping is parabolic in the fraction of Stern layer water molecules flipped and comparable to the cohesive energy of water and ice, depending on the choice of the Stern layer relative permittivity (2 and 1.33, respectively).

Probing interfacial solvent structure and electrostatic fields at electrode:electrolyte interfaces directly, in real time, and without the need for electrochemical, spin, or spectroscopic

labels, or plasmonic structures, remains a major challenge despite the topic's importance for many electrochemical transformations.[4,10-21] Consider the amphoteric nature of the oxides that terminate many electrodes used for the oxygen evolution reaction (OER). This reaction is typically carried out above the point of zero charge at high pH[14] where, at open circuit potential, the interfacial water molecules direct their protons to the electrode surface. In this configuration, access of the electrode's active sites to the electrons in water's oxygen atoms would be blocked by water's protons unless the applied potential is sufficiently high to weaken the interfacial hydrogen bond network so that the water molecules can flip to point their electron source (the oxygen atoms) towards the electrode's active site (the metal oxo site). The sensitivity of nonlinear optical processes to interfacial structure and electrostatics should make it possible to gain insights into Stern layer water flipping if the strong absorber problem could be overcome.

Prior nonlinear optical studies of electrode:electrolyte interfaces have largely been based on second harmonic generation (SHG) intensity measurements (see Gruen's[22] and Nagy and Roy's[23] pioneering work on nickel electrodes), from which $\Phi(0)_{tot}$ and $\chi^{(2)}$ cannot be quantified. Recent approaches have focused on potential-of-zero charge quantifications via SHG amplitude and phase measurements on a platinum electrode,[9,24] without quantifying $\Phi(0)_{tot}$ and $\chi^{(2)}$. These studies hark back to nonlinear electroreflectance studies from silver electrodes that started with Bloembergen in 1967.[25] SHG signals from aqueous electric double layers were first reported by Wang in 1969.[26] Heinz and Shen employed electrochemical conditions,[27,28] Richmond,[29-34] Corn,[35,36] and Guyot-Sionnest[37] pioneered the method in chemistry as electric-field induced second harmonic, and Eisenthal established it for insulators.[38] The field grew[39-42] to include vibrational sum frequency generation (SFG) spectroscopy.[43-49] Homodyne-detected SFG spectroscopy and SHG microscopy imaging under electrochemical control have now been realized by the Campen

and Roke groups for Au electrodes in the electrochemical stability window as well as for the OER.[50-53] Liu and Shen reported phase-resolved nonlinear optical measurements of optically thin, gate-controlled Si:SiOx:water interfaces,[54] while the Suntivich group applied phase-sensitive SHG to Pt electrodes to identify potentials of zero charge.[9,24] We now build on these excellent studies by using optically transparent thin metal nanolayers for which we quantify the Stern layer structure and electrostatics at electrodes from SHG amplitude and phase measurements.

In the experiments, we begin with a ten-nanometer thin nickel layer deposited by physical vapor deposition onto a glass microscope slide that is subsequently placed into a custom-designed spectro-electrochemical cell (Fig. 1a, please see Methods) connected to an electrochemical workstation and probed by a femtosecond laser oscillator (80 fs, 1034 nm, 75.5 MHz). Using single photon counting, we record the SHG intensity simultaneously with the current density as a function of applied potential at pH 13 and 1 M ionic strength (NaCl). The SHG intensity is quadratic in input power (see Supporting Information Fig. S1a). We find SHG intensity minima that precede the potentials of the well-known Ni^{2+}/Ni^{3+} redox pair (Fig. 1b and Supporting Information Fig. S5), which follow the scan rate dependence documented elsewhere.[55]

To obtain the SHG amplitude and phase, we record SHG interference patterns generated by beating three SHG sources against one another: source 1 is the electrode:electrolyte interface (the "signal"), source 2 is a local oscillator ("LO", a 50 μm thin piece of z-cut α-quartz, like in our earlier work)[56-61], and source 3 is a reference oscillator ("RO", a second 50 μm thin piece of z-cut α-quartz oriented such that its azimuthal angle is 30° relative to that of the LO, which maximizes the SHG amplitude and sets the ROLO phase to 180°, as shown in Supporting Information Figures S2 and S3). The RO and LO bracket a phase shifting unit made of a 1 mm thin fused silica plate on a computerized rotating stage.[62-64] Fig. 1c shows the interference fringes detected for the

electrode + ROLO signal as we vary the applied potential between -0.3 V and +0.7 V vs Ag/AgCl, as well as the triplicate measurement of the ROLO-only configuration (SHG signal from electrode blocked using a long-pass filter). Several CVs with a wider voltage range are presented as well. Clear variations in amplitude and phase are observed, especially at high positive applied potential when compared to around zero applied potential.

We obtain the total interfacial potential, $\Phi(0)_{tot}$, and the second-order nonlinear susceptibility, $\chi^{(2)}$, as follows: We first determine the ROLO phase by blocking the SHG signal from the sample electrode with a long-pass filter and subtract it from the phase obtained when all three SHG sources are active to obtain the SHG phase of the sample electrode as $\varphi_{sig} = \varphi_{electrode+ROLO} - \varphi_{ROLO}$. Here, $\varphi_{electrode+ROLO}$ refers to the SHG phase obtained when all three SHG pulses are present at the detector, while φ_{ROLO} refers to the SHG phase obtained when the SHG signal from the electrode:electrolyte interface is blocked using a long-pass filter and only the two SHG pulses from the reference and the local oscillators are sent into the detector. We then normalize the SHG amplitude to the value at the open circuit potential (OCP, measured to be around -0.1 V vs Ag/AgCl in our cell). Fig. 2a shows that the SHG phase decreases with increasing applied potential in a sigmoidal fashion, while the amplitude goes through minima at the applied potentials that coincide with the SHG intensity minima seen in Fig. 1b. We then calibrate the SHG response from our optical window against the second-order nonlinear susceptibility of another z-cut α-quartz piece put in place of the electrolyte solution like in our previous work,[56-59,61] accounting for Fresnel coefficients and the wave vector mismatch in our experimental geometry (please see Supporting Information Note S1). We then employ our recently established optical model for quantifying $\Phi(0)_{tot}$ and $\chi^{(2)}$ from the SHG amplitude and phase measured at silica:water interfaces for high ionic strength,[59,65] adding to it the metal-specific contributions to the second-order nonlinear

susceptibility discussed earlier by Guyot-Sionnest et al. (for Ag)[66] and Nagy and Roy (for Ni).[67] We obtain the following expression for the total potential drop across the electrode:electrolyte interface (see Supporting Information Note S1):

$$\Phi(0)_{tot} = \frac{C \cdot E_{sig,norm}\{sin(-\varphi_{sig}-90°)-5\cdot cos(-\varphi_{sig}-90°)\}}{(1.5-5)\chi^{(3)}_{water}} \qquad (1)$$

Here, C is the calibration factor that also accounts for the Fresnel coefficients (C=3.1 x 10^{-22} m^2V^{-1} in our case, please see Supplementary Information Note S1), $E_{sig,norm}$ is the measured SHG amplitude normalized to the value obtained at zero applied volt (the condition at which we calibrate to quartz, as described in Supplementary Information Note S1), φ_{sig} is given as explained above, and $\chi^{(3)}_{water}$ (1x10^{-21} m^2V^{-2} from experiment and theory, *vide infra*)[68,69] is the third-order nonlinear susceptibility of the diffuse layer, which has been shown to be invariant with ionic strength, pH, and surface composition.[70] Eqn. 1 accounts for the 90° phase shift from metals[64] and the *ca*. 5x larger nonlinear optical response we obtain from the nickel nanolayer when compared to a fused silica window, both at pH 13 and 1 M ionic strength (please see Supplementary Information Note S1). This experimentally determined factor of 5 is in good agreement with the computed factor of 4.5 in eqn. 7 of Nagy and Roy and the 1/2 term in eqn. 1 of Guyot-Sionnest et al. that account for metals' bulk magnetic dipole contribution to $\chi^{(2)}$.[66,67] With eqn. 1 establishing $\Phi(0)_{tot}$, the second-order nonlinear susceptibility is given by (see Supporting Information Note S1)

$$\chi^{(2)} = \left\{C \cdot E_{sig,norm} sin(-\varphi_{sig} - 90°) - 1.5 \cdot \Phi(0)_{tot} \cdot \chi^{(3)}_{water}\right\}/5 \qquad (2)$$

At $\Phi(0)_{tot}$=0, we find that $\chi^{(2)}_{\Phi(0)_{tot}=0V}$ is -4.8 x 10^{-22} ± 0.3 x 10^{-22} m^2V^{-1}. This non-zero value is attributed to the net aligned dipoles from the interfacial NiOH, NiO^-, and $NiOH_2^+$ groups. As these groups cannot flip their net orientation, we employ $\chi^{(2)}_{\Phi(0)_{tot}=0V}$ as the reference value relative to which we provide the change in the second-order nonlinear susceptibility, $\Delta\chi^{(2)}$, that arises when

the mobile Stern layer species change their orientation distribution in the presence of a non-zero total potential. Positively (*resp.*, negatively) signed values of $\Delta\chi^{(2)}$ correspond to water molecules pointing their protons towards from (*resp.*, away from) the electrode, consistent with SHG and SFG result from colloidal[68] and macroscopically flat[59,71,72] oxide/water interfaces.

Fig. 2b shows the total potential and the second-order nonlinear susceptibility obtained from eqns. 1 and 2 as a function of externally applied potential. At open circuit potential, the total potential is between -300 mV and -350 mV, consistent with the negative surface charge of nickel oxide at pH 13 (points of zero charge of nickel oxides are below pH 11).[73-76] We note that this total potential is the Gouy-Chapman-Stern potential associated with the mobile charges (ions) plus the contributions from the immobile charges (electrons bound to the molecules and ions), like from dipoles and quadrupoles. The total potential first decreases in magnitude with increasingly positive applied potential until it crosses 0 V at +0.4 V potential applied vs Ag/AgCl at pH 13. At this applied voltage, the electrode is at the potential of zero charge, which coincides with the minimum observed in the SHG intensity vs applied potential run shown in Fig. 1b. Fig. 2b also shows that the net-change in the second-order nonlinear susceptibility becomes smaller as the applied potential becomes more positive. At the point of zero total potential ($\Phi(0)_{tot}$=0), $\Delta\chi^{(2)}$ is zero, indicating a lack of symmetry breaking (the key requirement for a non-zero $\chi^{(2)}$ value) that is consistent, to leading order, with an isotropic arrangement of the Stern layer water molecules (equal number of interfacial water molecules with dipole moments pointing up and down, or all fully disordered, so that $\mathcal{N}\cdot\langle\alpha^{(2)}\rangle$=0, where $\mathcal{N}$ is the total number of Stern layer water molecules and $\alpha^{(2)}$ is water's molecular hyperpolarizability). Fig. 2c shows that similar results are obtained when using NaOH, KOH, and CsOH, as well as different fringe acquisition times, while Fig. 2d shows the variation of $\Phi(0)_{tot}$=0 and $\Delta\chi^{(2)}$ for a slightly wider range of applied potentials.

Encouraged by these results, we proceeded to estimate the number of water molecules that flip their dipole orientations. To this end, we employed the molecular hyperpolarizability for a liquid water model estimated by Gubskaya and Kusalik at the MP2 and MP4 level of theory ($\alpha^{(2)}$=5.3 x 10^{-52} C m^3V^{-2}).[77] This value was used recently by the Roke group[68] to estimate the third-order nonlinear susceptibility, $\chi^{(3)}$, of liquid water, which is in good agreement with the experimental value reported by Dalstein et al.[69] Dividing the $\Delta\chi^{(2)}$ values shown in Fig. 2b-d by $\alpha^{(2)}$ and multiplying by a Stern layer water permittivity estimate (ε=1.33 to 2)[78] then yields the number of water molecules per cm^2 that flip their orientation.

Fig. 3a shows that at the most positive applied potential (+0.9 V), ca. 1.1 x 10^{15} water molecules have a net orientation with protons pointing away from the electrode (we denote that number of molecules with a negative sign in the figure). This value is the upper estimate of the Stern layer water density, $\mathcal{N}_{water\downarrow, max}$, given it is obtained from the lower bound of the relative permittivity, so the actual $\mathcal{N}_{water\downarrow, max}$ is likely less given the range in reported values for the relative permittivity in the Stern layer.[56,78-85] Yet, our range of $\mathcal{N}_{water\downarrow, max}$ estimates using ε=1.33 to 2 (1.1 x 10^{15} cm^{-2} to 0.8 x 10^{15} cm^{-2}, respectively) is close to the geometric number density of water molecules on the surface of a 1 cm^3 cube of liquid water at standard temperature and pressure (1 x 10^{15} cm^{-2}). Most if not all the Stern layer water molecules pointing their oxygen atoms towards the electrode at this applied voltage would be consistent with a relative permittivity of 1.33 for the Stern layer water molecules. The number of net-aligned water molecules is about five times smaller at the negative applied potentials surveyed when compared to positive potential. Computing the electric field across the electrode:electrolyte interface by dividing the total potential by the Debye length at the high ionic strength employed here (0.7 nm at 1 M) shows that all the Stern layer water molecules that have flipped are subject to a field of close to -1 x 10^7 V cm^{-1} (top

x-axis in Fig. 3a). We then compute the total interfacial energy by multiplying the total potential by the elemental charge and the number of oriented Stern layer water molecules (Fig. 3b). We find a parabolic variation of the free energy with the fraction of Stern layer water molecules pointing their oxygen atoms towards the electrode. The energies range from 43 to 65 kJ mol^{-1}, depending on the choice of relative permittivity. The lower point estimate is close to the cohesive energy of liquid water (44.5 kJ mol^{-1})[86] while the upper is near that of ice (59 kJ mol^{-1}).[87] The experimental data can be modeled with a 2-dimensional Ising model describing Stern layer water molecules pointing their oxygen atoms towards and away from the electrode. Employing the Helmholtz free energy mean field solution for the square lattice model (z=4)[88]

$$f = (\mathcal{N}_{\mathrm{water}\downarrow})^2 J\frac{z}{2} - \beta^{-1} ln\left[cosh\left(\beta \cdot (Jz|\mathcal{N}_{\mathrm{water}\downarrow}| + e \cdot \Phi_{tot})\right)\right] \quad (3),$$

where $\mathcal{N}_{\mathrm{water}\downarrow}$= – 1 x 10^{13} – Φ_{tot} x 1 x 10^{15} (the linear least squares fit result of the ε=1.33 dataset shown in Fig. 3b), J is the coupling constant, β=(k_BT)$^{-1}$ with k_B being the Boltzmann constant and T being temperature (300K), and e is the elementary charge. This model is consistent with coupling constants of -1.2 x 10^{-34} J and -0.8 x 10^{-34} J for the ca. 1 x 10^{15} water molecules in the Stern layer assuming ε=1.33 and ε=2.0, respectively, for the relative permittivity.

In conclusion, we report the implementation of a second harmonic generation pulse triplet from which the SHG amplitude and phase are determined for a nickel electrode:electrolyte interface maintained at pH 13 and externally potentials ranging from -0.5 to +0.9 V against Ag/AgCl. Employing calibration procedures using z-cut α-quartz we quantify the drop of the total potential, Φ_{tot}, across the interface as well as the second order nonlinear susceptibility, $\chi^{(2)}$. We find that the interfacial electrostatics and structure vary sigmoidally with applied potential while they vary linearly when plotted against one another. The potential of zero Φ_{tot} is around +0.4V vs Ag/AgCl at pH 13 and 1 M ionic strength (near the SHG intensity minimum shown in Fig. 1b),

which is the potential of zero charge. Employing commonly used estimates for the relative permittivity in the Stern layer, we find that the changes in $\chi^{(2)}$ with externally applied potential correspond to net-aligned water molecules, $\mathcal{N}_{water\downarrow, max}$, of 0.9 x 10^{15} cm^{-2} to 1.1 x 10^{15} cm^{-2} at the highest potentials applied (+0.7 to +0.9V vs Ag/AgCl). A two-dimensional Ising model applied to the number of net-aligned water molecules, $\mathcal{N}_{water\downarrow}$, as a function of Φ_{tot} recapitulates the experimentally derived variation of $\mathcal{N}_{water\downarrow}$ with Φ_{tot}, while the energy density associated with aligning all the Stern layer water molecules at high positive applied potential ranges between the cohesive energies or ice and water, depending on the choice of the Stern layer relative permittivity. We expect that fundamental advances and insights like the ones presented here will be useful for the ongoing rapid development of molecular electrochemistry.

Methods. The electrochemical workstation is a Metrohm Autolab model (PGSTAT302N), where the working electrode is in contact with aqueous electrolyte having the ionic strengths and pH value indicated in the main text. We employ a Pt counter reference electrode and a Ag:AgCl reference electrode in a frit. FKM O-rings are used for sealing the spectro-electrochemical cell, which is unstirred and consists of a double-paned custom-designed assembly (redox.me) manufactured from PEEK (please see Supporting Information Fig. S1b). The open circuit potential is measured before each electrochemical experiment to be -0.1 V ± 0.03 V (vs Ag/AgCl, at pH 13, 1 M ionic strength, average of several score electrodes). One window consists of a standard 1 inch x 3 inch VWR microscope glass slide onto which a ten-nm thin nickel nanolayer is deposited using a physical vapor deposition method described earlier that minimizes low-boiling point impurities (K, Ca, Mg).[89] X-ray photoelectron spectroscopy shows the presence of nickel oxide on the electrode surface.[89] The second window is a fused silica window that allows for the incident laser pulses at the fundamental frequency to exit the electrochemical assembly towards a beam stop.

Alkaline solutions of NaOH and KOH are used at pH 13 with NaCl and KCl added to bring them to 1 mol L^{-1} concentration. Each solution is prepared with pure Millipore water (18.2 MΩ·cm), allowed to equilibrate overnight, and then the pH was measured. NaOH (Lot no. B0312669941, Part no. SX0590-1500g, >97% pure) was purchased from EMD Chemicals, NaCl (Lot no. M08A016, Part no. 12314-36, >99% purity) was purchased from Alfa Aesar, KOH (Lot no. MKCS8606, Part no. 306568-100g, 99.99% trace metal basis) was purchased from Sigma-Aldrich, and KCl (Lot no. LBP3785V, Part no. 746435-500g, ≥99% purity) was purchased from Sigma Aldrich as well. The scan rate dependent potential differences of the $Ni^{2/3+}$ oxidation and reduction peaks (Supporting Information Fig. S5) are in good agreement with Fe salt-free results shown in Fig. 2i of ref. 55.

We direct 0.2 W from a LightConversion Flint oscillator (model FL1-02) producing 80 femtosecond pulses at 1034 nm at a 75.5 MHz repetition rate onto the electrode:electrolyte interface using a defocused (-1 cm) 10 cm lens (spot size *ca*. 100 μm diameter) and block the reflected fundamental light from the air:window interface. We direct the SHG pulses along with the reflected fundamental pulses from the electrode:electrolyte interface towards an off-axis parabolic mirror (Thorlabs) and an uncoated 0.5 mm thin a-cut calcite time delay compensator (CAL12050-A, Newlight Photonics) to account for spatial and temporal dispersion at the detector, as described in our earlier work.[65] Here, we send the pulses at the fundamental and the second harmonic frequency first through a 50 um thin z-cut a-quartz window (producing the reference oscillator, RO, (Precision Micro-Optics PWQB-368252), then a 1 mm thin fused silica phase shifting unit (ISP Optics) on a rotating stage (Standa model 8MR174-11), and then a second 50 um thin z-cut a-quartz window (producing the local oscillator, LO). The SHG pulse triplet (signal+RO+LO) then passes through a notch-filter centered at the SHG wavelength and interferes

at the detector (Hamamatsu H8259-01) as a function of the phase shifting unit (PSU) angle, which we vary by 40° around the normal in 1° steps. We record the SHG signal with a 100 ms acquisition time and 5-, 10-, and 20-fold averaging at each PSU angle. This data acquisition scheme then results in 40, 80, and 160 sec time periods per complete fringe, not counting the resetting of the rotational stage to the starting angle (a few seconds). We record three fringes at each applied potential and fit the 3rd fringe to the following expression from Stolle and Marowsky:[63]

$$f(\gamma)=K_0+K_2\cdot(\gamma-\delta\gamma)^2+Esig\cdot\{\cos[4\cdot\pi\cdot(d/(1.03\cdot10^{-6}))\cdot [n\cdot1.4619\cdot\cos(\text{asin}\{\sin[(((\gamma-\delta\gamma))\cdot\pi/180)/(n\cdot1.4619)]\})- 1.4501\cdot\cos(\text{asin}(\sin((((\gamma-\delta\gamma))\cdot\pi\ /180)/1.4501)))]+\varphi_{sig}\cdot\pi/180)\} \quad (4)$$

Here, γ-δγ is the PSU angle and its small offset (typically around ±1°) that accounts for imperfections in zeroing the PSU plate angle as well as slight motor backlash. We employ a 4-parameter Cauchy fit to the refractive index data for the infrared-grade fused silica from ISP optics to obtain the necessary refractive indices at the fundamental and SHG wavelengths. A caliper was used to determine the actual fused silica plate thickness, *d*, to be 1.07566 mm. The refractive index of air, *n*, is taken to be 1.0003. We then subtract the phase of the ROLO-only SHG doublet (obtained by blocking the SHG signal using a long-pass filter, $\varphi_{signal+ROLO.}-\varphi_{ROLO}$) to obtain the signal (i.e., electrode:electrolyte interface) SHG phase. Replicate measurements are performed using various laser spot positions on a given nickel electrode, as well as with various different electrodes so as to account for variations in the measurements that come along with slight variations in how the sample cell is assembled and mounted between replicates/trials (please see Supporting Information Fig. S3c-f for majority and minority responses in the SHG amplitude and phase from various parts on a given nickel electrode).

Acknowledgments

This work was supported by the US National Science Foundation (CHE-2153191), the Air Force Office of Scientific Research (FA9550-16-1-0379), the Department of Energy (DE-SC0023342), and the Army Research Office/Defense Advanced Research Program Agency (W911NF1910361/75506-CH-DRP). FMG designed the experiment. RS and FMG carried out the experiments, analyzed the data, and wrote the manuscript.

References

1 Vatamanu, J. & Borodin, O. Ramifications of Water-in-Salt Interfacial Structure at Charged Electrodes for Electrolyte Electrochemical Stability. *J. Phys. Chem. Lett.* **8**, 4362-4367 (2017).

2 Magnussen, O. M. & Gross, A. Toward an Atomic-Scale Understanding of Electrochemical Interface Structure and Dynamics. *J. Am. Chem. Soc.* **141**, 4777-4790 (2019).

3 Zhang, C., Hutter, J. & Sprik, M. Coupling of Surface Chemistry and Electric Double Layer at TiO2 Electrochemical Interfaces. *J. Phys. Chem. Lett.* **10**, 3871-3876 (2019).

4 Zhang, Y., de Aguiar, H. B., Hynes, J. T. & Laage, D. Water Structure, Dynamics, and Sum-Frequency Generation Spectra at Electrified Graphene Interfaces. *J. Phys. Chem. Lett.* **11**, 624-631 (2020).

5 Rossmeisl, J. *et al.* Realistic Cyclic Voltammograms from Ab Initio Simulations in Alkaline and Acidic Electrolytes. *J. Phys. Chem. C* **124**, 20055-20065 (2020).

6 Sakong, S. & Groß, A. Water structures on a Pt(111) electrode from ab initio molecular dynamic simulations for a variety of electrochemical conditions. *Phys. Chem. Chem. Phys.* **22**, 10431-10437 (2020).

7 Piontek, S. M. *et al.* Probing Heterogeneous Charge Distributions at the α-Al2O3(0001)/H2O Interface. *J. Am. Chem. Soc.* **142**, 12096-12105 (2020).

8 Ge, A. *et al.* On the Coupling of Electron Transfer to Proton Transfer at Electrified Interfaces. *J. Am. Chem. Soc.* **142**, 11829-11834 (2020).

9 Xu, P., von Rueden, A. D., Schimmenti, R., Mavrikakis, M. & Suntivich, J. Optical method for quantifying the potential of zero charge at the platinum-water electrochemical interface. *Nature Materials* **22**, 503-510 (2023).

10 Jayaraman, S., May, E. L. & Hillier, A. C. Scanning Electrochemical Mapping of Spatially Localized Electrochemical Reactions Induced by Surface Potential Gradients. *Langmuir* **22**, 10322-10328 (2006).

11 Voinov, M. A., Rivera-Rivera, I. & Smirnov, A. I. Surface electrostatics of lipid bilayers by EPR of a pH-sensitive spin-labeled lipid. *Biophys. J.* **104**, 106-116 (2013).

12 McBriarty, M. E., Stubbs, J. E., Eng, P. J. & Rosso, K. M. Potential-Specific Structure at the Hematite–Electrolyte Interface. *Adv. Functional Mat.* **28**, 1705618 (2017).

13 Liang, Z., Ahn, H. S. & Bard, A. J. A Study of the Mechanism of the Hydrogen Evolution Reaction on Nickel by Surface Interrogation Scanning Electrochemical Microscopy. *J. Am. Chem. Soc.* **139**, 4854-4858 (2017).

14 Song, F. *et al.* Transition Metal Oxides as Electrocatalysts for the Oxygen Evolution Reaction in Alkaline Solutions: An Application-Inspired Renaissance. *J. Am. Chem. Soc.* **140**, 7748-7759 (2018).

15 Nellist, M. R. *et al.* Potential-sensing electrochemical atomic force microscopy for in operando analysis of water-splitting catalysts and interfaces. *Nat. Energy* **3**, 46-52 (2018).

16 Wang, Y., Cao, Z., Yang, Q., Guo, W. & Su, B. Optical methods for studying local electrochemical reactions with spatial resolution: A critical review. *Anal. Chim. Acta* **1074**, 1-15 (2019).

17 Sarabia, F. J., Sebastián-Pascual, P., Koper, M. T. M., Climent, V. & Feliuy, J. M. Effect of the Interfacial Water Structure on the Hydrogen Evolution Reaction on Pt(111) Modified

with Different Nickel Hydroxide Coverages in Alkaline Media. *ACS Appl. Mater. Interfaces* **11**, 613-623 (2019).

18 Kulesza, P. J. & Rutkowska, I. A. Future of interfacial electrochemistry: from structure-function relationships to better understanding of charge transfer reactions and (photo)electrocatalytic reactivity. *J. Solid State Electrochem.* **24**, 2115-2116 (2020).

19 Gonella, G. *et al.* Water at charged interfaces. *Nature Reviews Chemistry* **5**, 466-485 (2021). https://doi.org:10.1038/s41570-021-00293-2

20 Futera, Z. & English, N. J. Water Breakup at Fe2O3−Hematite/Water Interfaces: Influence of External Electric Fields from Nonequilibrium Ab Initio Molecular Dynamics. *J. Phys. Chem. Lett.* **12**, 6818-6826 (2021).

21 Shin, S.-J. *et al.* On the importance of the electric double layer structure in aqueous electrocatalysis. *Nature Comm.* **13**, 174 (2022).

22 Biwer, B. M., Pellin, M. J., Schauer, M. W. & Gruen, D. M. Electrochemical and Second Harmonic Generation Investigation of Nickel Corrosion in 0.1 M NaOH. *Surf. Interf. Anal.* **14**, 635-646 (1989).

23 Nagy, G. & Roy, D. Second harmonic generation from a charged Ni electrode with and without anion adsorption. *Surf. Sci.* **320**, 7-16 (1994).

24 Xu, P., Huang, A. & Suntivich, J. Phase-Sensitive Second-Harmonic Generation of Electrochemical Interfaces. *J. Phys. Chem. Lett.* **11**, 8216-8221 (2020).

25 Lee, C. H., Chang, R. K. & Bloembergen, N. Nonlinear Electroreflectance in Silicon and Silver. *Phys. Rev. Lett.* **18**, 167-170 (1967).

26 Wang, C. Second-Harmonic Generation of Light at the Boundary of an Isotropic Medium. *Phys. Rev.* **178**, 1457-1461 (1969).

27 Heinz, T. F., Chen, C. K., Ricard, D. & Shen, Y. R. Optical 2nd-Harmonic Generation from a Monolayer of Centrosymmetric Molecules Adsorbed on Silver. *Chemical Physics Letters* **83**, 180-182 (1981).

28 Chen, C. K., Heinz, T. F., Ricard, D. & Shen, Y. R. Surface-Enhanced 2nd-Harmonic Generation and Raman-Scattering. *Phys. Rev. B* **27**, 1965-1979 (1983).

29 Richmond, G. L. Surface second harmonic generation from sulfate ions adsorbed on silver electrodes. *Chem. Phys. Lett.* **106**, 26-29 (1984).

30 Rojhantalab, H. M. & Richmond, G. L. Interfacial Studies of Silver-Aqueous Electrolytes by Optical 2nd Harmonic and Differential Capacitance. *Journal of the Optical Society of America a-Optics Image Science and Vision* **3**, P52-P53 (1986).

31 Richmond, G. L. Characterization of the Silver Aqueous-Electrolyte Interface by Optical 2nd Harmonic-Generation. *Langmuir* **2**, 132-139 (1986).

32 Richmond, G. L. Adsorption of ions on smooth and roughened silver surfaces: a comparative study by optical second harmonic generation. *Chemical Physics Letters* **113**, 359-363 (1985).

33 Richmond, G. L., Rojhantalab, H. M., Robinson, J. M. & Shannon, V. L. Experiments on optical second-harmonic generation as a surface probe of electrodes. *J. Opt. Soc. Am. B-Opt. Phys.* **4**, 228-236 (1987).

34 Richmond, G. L. Insitu Characterization of Solid Liquid Interfaces by Optical 2nd Harmonic-Generation. *Journal of the Electrochemical Society* **134**, C111-C111 (1987).

35 Corn, R. M., Romagnoli, M., Levenson, M. D. & Philpott, M. R. The Potential Dependence of Surface Plasmon-Enhanced Second-Harmonic Generation at Thin Film Silver Electrodes. *Chem. Phys. Lett.* **106**, 30-35 (1984).

36 Lantz, J. M. & Corn, R. M. Time-Resolved Optical Second Harmonic Generation Measurements of Picosecond Band Flattening Processes at Single Crystal Ti02 Electrodes. *J. Phys. Chem.* **98**, 9387-9390 (1994).

37 Guyot-Sionnest, P. & Tadjeddine, A. Study of Ag(111) and Au(111) Electrodes by Optical Second-harmonic Generation. *J. Chem. Phys.* **92**, 734-738 (1990).

38 Ong, S., Zhao, X. & Eisenthal, K. B. Polarization of water molecules at a charged interface; second harmonic studies of the silica/water interface. *Chem. Phys. Lett.* **191**, 327-335 (1992).

39 Richmond, G. L., Robinson, J. M. & Shannon, V. L. 2nd Harmonic-Generation Studies of Interfacial Structure and Dynamics. *Progress in Surface Science* **28**, 1-70 (1988).

40 Corn, R. M. & Higgins, D. A. Optical Second Harmonic Generation as a Probe of Surface Chemistry. *Chem. Rev.* **94**, 107 (1994).

41 Eisenthal, K. B. Liquid interfaces probed by second-harmonic and sum-frequency spectroscopy. *Chem. Rev.* **96**, 1343-1360 (1996).

42 Eisenthal, K. B. Second Harmonic Spectroscopy of Aqueous Nano- and Microparticle Interfaces *Chem. Rev.* **106**, 1462-1477 (2006).

43 Baldelli, S., Markovic, N., Ross, P., Shen, Y. R. & Somorjai, G. Sum frequency generation of CO on (111) and polycrystalline platinum electrode surfaces: Evidence for SFG invisible surface CO. *J. Phys. Chem. B* **103**, 8920-8925 (1999).

44 Baldelli, S., Mailhot, G., Ross, P., Shen, Y. R. & Somarjai, G. A. Potential dependent orientation of acetonitrile on platinum (111) electrode surface studied by sum frequency generation. *Journal of Physical Chemistry B* **105**, 654-662 (2001).

45 Baldelli, S. Probing Electric Fields at the Ionic Liquid-Electrode Interface Using Sum Frequency Generation Spectroscopy and Electrochemistry. *J. Phys. Chem. B* **109**, 13049-13051 (2005).

46 Shaw, S. K., Lagutchev, A., Dlott, D. D. & Gewirth, A. A. Electrochemically Driven Reorientation of Three Ionic States of p-Aminobenzoic Acid on Ag(111). *The Journal of Physical Chemistry C* **113**, 2417-2424 (2009). https://doi.org:10.1021/jp808445q

47 Shaw, S. K., Lagutchev, A., Dlott, D. D. & Gewirth, A. A. Sum-Frequency Spectroscopy of Molecular Adsorbates on Low-index Ag Surfaces: Effects of Azimuthal Rotation. *Analytical Chemistry* **81**, 1154-1161 (2009). https://doi.org:10.1021/ac802332h

48 Garcia Rey, N. & Dlott, D. D. Structural Transition in an Ionic Liquid Controls CO2 Electrochemical Reduction. *J. Phys. Chem. C* **119**, 20892-20899 (2015).

49 Garcia Rey, N. & Dlott, D. D. Studies of electrochemical interfaces by broadband sum frequency generation. *J. Electroanal. Chem.* **800**, 114-125 (2017).

50 Tong, Y., Cai, K., Wolf, M. & Campen, R. K. Probing the electrooxidation of weakly adsorbed formic acid on Pt(1 0 0). *Catalysis Today* **260**, 66-71 (2016).

51 Tong, Y., Lapointe, F., Thaemer, M., Wolf, M. & Campen, R. K. Experimentally Probing Hydrophobic Water at the Gold Electrode / Aqueous Interface. *Angew. Chemie Int. Ed.* **56**, 4211-4214 (2017).

52 Nahalka, I., Zwaschka, G., Campen, R. K., Marchioro, A. & Roke, S. Mapping Electrochemical Heterogeneity at Gold Surfaces: A Second Harmonic Imaging Study. *J. Phys. Chem. C* **124**, 20021-20034 (2020).

53 Zwaschka, G. *et al.* Imaging the Heterogeneity of the Oxygen Evolution Reaction on Gold Electrodes Operando: Activity is Highly Local. *ACS Catalysis* **10**, 6084-6093 (2020).

54 Wang, H. *et al.* Gate-Controlled Sum-Frequency Vibrational Spectroscopy for Probing Charged Oxide/Water Interfaces. *J. Phys. Chem. Lett.* **10**, 5943-5948 (2019).

55 Akbari, M. S. A., Bagheri, R., Song, Z. & Najafpour, M. M. Oxygen-evolution reaction by nickel/nickel oxide interface in the presence of ferrate (Vi). *Sci. Rep.* **10**, 8757 (2020).

56 Boamah, M. D., Ohno, P. E., Geiger, F. M. & Eisenthal, K. B. Relative permittivity in the electrical double layer from nonlinear optics. *J. Chem. Phys.* **148**, 222808 (2018).

57 Boamah, M. D., Ohno, P. E., Lozier, E., Van Ardenne, J. & Geiger, F. M. Specifics about Specific Ion Adsorption from Heterodyne-Detected Second Harmonic Generation. *Journal of Physical Chemistry B* **123**, 5848-5856 (2019). https://doi.org:10.1021/acs.jpcb.9b04425

58 Chang, H., Ohno, P. E., Liu, L. & Geiger, F. M. Direct Measurement of Charge Reversal on Lipid Bilayers using Heterodyne-Detected Second Harmonic Generation Spectroscopy. *J. Phys. Chem. B* **124** (2020).

59 Ma, E. *et al.* A New Imaginary Term in the 2nd Order Nonlinear Susceptibility from Charged Interfaces. *J. Phys. Chem. Lett.* **12**, 5649-5659 (2021). https://doi.org:10.26434/chemrxiv.14378810.v1

60 Ma, E. *et al.* Stern and Diffuse Layer Interactions during Ionic Strength Cycling. *Journal of Physical Chemistry C* **125**, 18002-18014 (2021). https://doi.org:10.1021/acs.jpcc.1c04836

61 Ma, E. & Geiger, F. M. Divalent Ion Specific Outcomes on Stern Layer Structure and Total Surface Potential at the Silica:Water Interface. *Journal of Physical Chemistry A* **125**, 10079-10088 (2021). https://doi.org:10.1021/acs.jpca.1c08143

62 Huang, J. Y. & Lewis, A. Determination of the absolute orientation of the retinylidene chromophore in purple membrane by a second-harmonic interference technique. *Biophys. J.* **55**, 835-842 (1989).

63 Stolle, R., Marowsky, G., Schwarzberg, E. & Berkovic, G. Phase measurements in nonlinear optics. *Appl. Phys. B* **63**, 491-498 (1996).

64 Covert, P. A. & Hore, D. K. Assessing the Gold Standard: The Complex Vibrational Nonlinear Susceptibility of Metals. *J. Phys. Chem. C* **119**, 271-276 (2014).

65 Ohno, P. E. *et al.* Beyond the Gouy–Chapman Model with Heterodyne-Detected Second Harmonic Generation. *J. Phys. Chem. Lett.* **10**, 2328-2334 (2019).

66 Guyot-Sionnest, P., Tadjeddine, A. & Liebsch, A. Electronic Distributions and Nonlinear Optical Response at the Metal-Electrolyte Interface. *Phys. Rev. Lett.* **64**, 1678-1681 (1990).

67 Nagy, G. & Roy, D. Surface charge dependence of second harmonic generation from a Ni electrode. *Chem. Phys. Lett.* **214**, 197-202 (1993).

68 Lütgebaucks, C., Gonella, G. & Roke, S. Optical label-free and model-free probe of the surface potential of nanoscale and microscopic objects in aqueous solution. *Phys. Rev. B* **94**, 195410 (2016). https://doi.org:10.1103/PhysRevB.94.195410

69 Dalstein, L., Chiang, K.-Y. & Wen, Y.-C. Direct Quantification of Water Surface Charge by Phase-Sensitive Second Harmonic Spectroscopy. *The Journal of Physical Chemistry Letters* **10**, 5200-5205 (2019). https://doi.org:10.1021/acs.jpclett.9b02156

70 Wen, Y.-C. *et al.* Unveiling Microscopic Structures of Charged Water Interfaces by Surface-Specific Vibrational Spectroscopy. *Physical Review Letters* **116**, 016101 (2016).

71 Rehl, B. *et al.* Water Structure in the Electrical Double Layer and the Contributions to the Total Interfacial Potential at Different Surface Charge Densities. *J. Am. Chem. Soc.* **144**, 16338-16349 (2022).

72 Wei, F., Urashima, S.-h., Nihongyanagi, S. & Tahara, T. Elucidation of the pH-Dependent Electric Double Layer Structure at the Silica/Water Interface Using Heterodyne-Detected Vibrational Sum Frequency Generation Spectroscopy. *J. Am. Chem. Soc.* **145**, 8833-8846 (2023).

73 Parks, G. A. Isoelectric Points of Solid Oxides Solid Hydroxides and Aqueous Hydroxo Complex Systems. *Chem. Rev.* **65**, 177-& (1965).

74 Tewari, P. H. & Campbell, A. B. Temperature Dependenceof Pointof Zero Chargeof Cobalt and Nickel Oxidesand Hydroxides. *J. Coll. Int. Sci.* **55**, 531-539 (1976).

75 Kosmulski, M. The pH-dependent surface charging and points of zero charge: V. Update. *Journal of Colloid and Interface Science* **353**, 1-15 (2011). https://doi.org:http://dx.doi.org/10.1016/j.jcis.2010.08.023

76 Mahmood, T. *et al.* Comparison of Different Methods for the Point of Zero Charge Determination of NiO. *Industrial & Engineering Chemistry Research* **50**, 10017-10023 (2011). https://doi.org:10.1021/ie200271d

77 Gubskaya, A. V. & Kusalik, P. G. The multipole polarizabilities and hyperpolarizabilities of the water molecule in liquid state: an ab initio study. *Mol. Phys.* **99**, 1107-1120 (2001).

78 Fumagalli, L. *et al.* Anomalously low dielectric constant of confined water. *Science* **360**, 1339-1342 (2018).

79 Kurosaki, S. The Dielectric Behavior of Sorbed Water on Silica Gel. *The Journal of Physical Chemistry* **58**, 320-324 (1954). https://doi.org:10.1021/j150514a009

80 Sakamoto, T., Nakamura, H., Uedaira, H. & Wada, A. High-frequency dielectric relaxation of water bound to hydrophilic silica gels. *The Journal of Physical Chemistry* **93**, 357-366 (1989). https://doi.org:10.1021/j100338a069

81 Sahai, N. & Sverjensky, D. A. Evaluation of internally consistent parameters for the triple-layer model by the systematic analysis of oxide surface titration data. *Geochimica Et Cosmochimica Acta* **61**, 2801-2826 (1997).

82 Teschke, O., Ceotto, G. & de Souza, E. F. Interfacial water dielectric-permittivity-profile measurements using atomic force microscopy. *Physical Review E* **64**, 011605 (2001).

83 Wander, M. C. F. & Clark, A. E. Structural and Dielectric Properties of Quartz−Water Interfaces. *The Journal of Physical Chemistry C* **112**, 19986-19994 (2008). https://doi.org:10.1021/jp803642c

84 Pilon, L., Wang, H. & d''Entremont, A. Recent Advances in Continuum Modeling of Interfacial and Transport Phenomena in Electric Double Layer Capacitors. *J. Electrochem. Soc.* **162**, A5158-5178 (2015).

85 Schlaich, A., Knapp, E. W. & Netz, R. R. Water Dielectric Effects in Planar Confinement. *Physical Review Letters* **117**, 048001 (2016).

86 Kirkham, M. B. in *Principles of Soil and Plant Water Relations* (ed M. B. Kirkham) (Academic Press, 2005).

87 Petrenko, V. F. & Whitworth, R. W. *Physics of Ice*. (Oxford University Press, 1999).

88 Codello, A. *Please see Chapter 5, Ising Model and Phase Transitions, in https://universalitylectures.wordpress.com*, 2013).

89 Boamah, M. D. *et al.* Energy Conversion via Metal Nanolayers. *PNAS* **116**, 16210-16215 (2019).

Figure Captions

Fig. 1 a) Top view of the beam path for the SHG pulse triplet. LPF=motorized long pass filter, OAP=off-axis parabolic mirror, TDC=time-delay compensator, RO=reference oscillator, PSU=motorized phase shifting unit, LO=local oscillator, SPF=short pass filter, PMT=photomultiplier tube. Beams offset for clarity. **b**) SHG intensity and current density recorded as a function of applied potential during three replicate cyclic voltammograms. **c**) Interference fringes recorded from the electrode:electrolyte interface, the reference oscillator, and the local oscillator (ROLO) as a function of applied potential and from the ROLO assembly only (SHG signal from electrode:electrolyte interface blocked with a long-pass filter).

Fig. 2. a) SHG Phase and intensity as a function of applied potential. **b**) Total potential, second order nonlinear susceptibility minus the second order nonlinear susceptibility obtained at zero total potential, and current density as a function of applied potential. **c**) Second order nonlinear susceptibility minus the second order nonlinear susceptibility obtained at zero total potential as a function of applied potential for pH 13 and 1 M ionic strength using Na^+ (green), K^+ (red), and Cs^+ (grey) as cations. **d**) Number of Stern layer water molecules having a net-orientation with their oxygen atoms pointed towards (*resp.*, away from) the electrode (negative and *resp.,* positive values) and their fraction, f, as a function of applied potential, computed using the color-coded Stern layer relative permittivities.

Fig. 3. a) Number of Stern layer water molecules having a net-orientation with their oxygen atoms pointed towards (*resp.*, away from) the electrode (negative and *resp.,* positive values) as a function of total potential and electric field, computed using the color-coded Stern layer relative permittivities. **b**) Total energy associated with water flipping as a function of the fraction of water molecules having a net-orientation with their oxygen atoms pointed towards the electrode,

computed using the color-coded Stern layer relative permittivities. Upper and lower bounds of shaded area indicate range of cohesive energies of water and ice, respectively. Light and dark red line indicate 2D-Ising model results with J=-1.2 x 10^{-34} J and J=-0.8 x 10^{-34} J.

Fig. 1

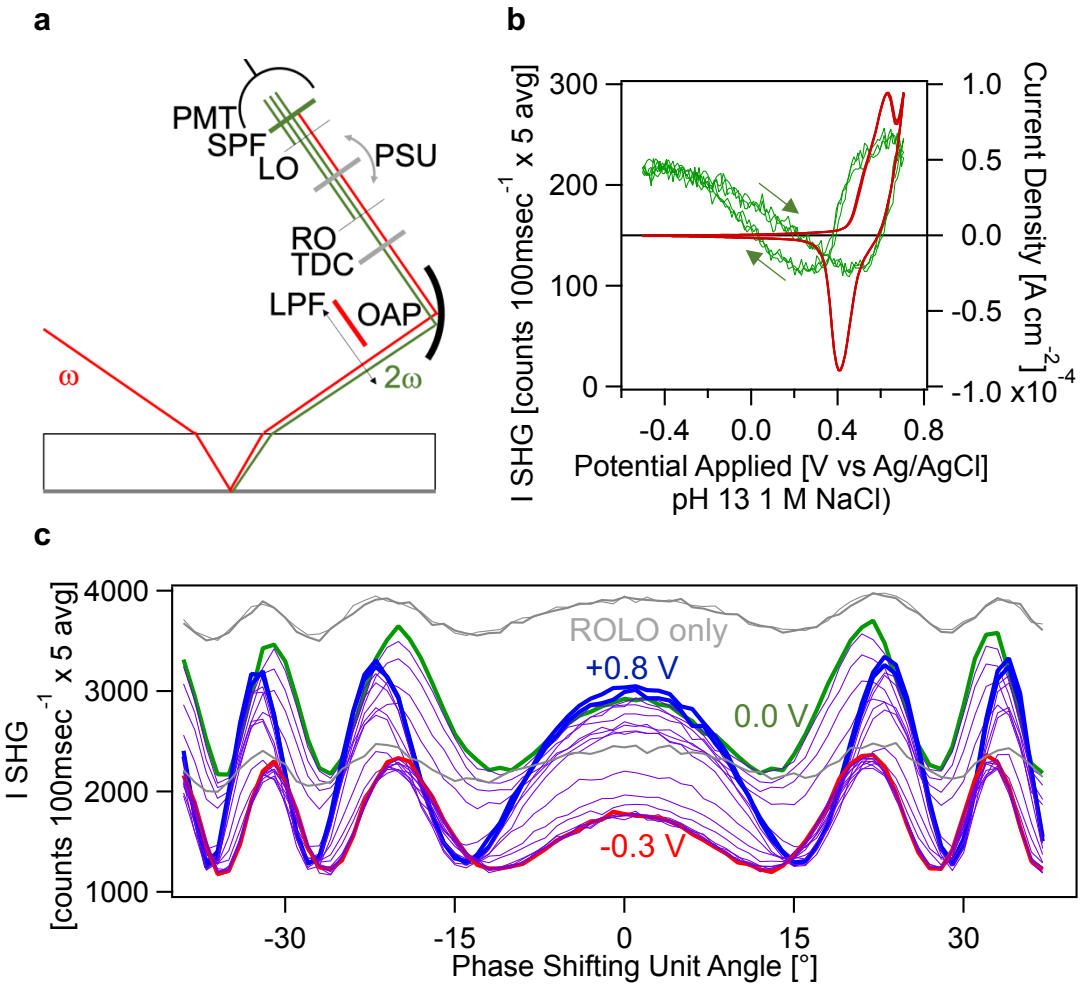
a
PMT
SPF
LO
PSU
RO
TDC
LPF
OAP
ω
2ω
b
I SHG [counts 100msec-1 x 5 avg]
Current Density [A cm-2] x10-4
Potential Applied [V vs Ag/AgCl]
pH 13 1 M NaCl)
c
I SHG
[counts 100msec-1 x 5 avg]
ROLO only
+0.8 V
0.0 V
-0.3 V
Phase Shifting Unit Angle [°]

Fig. 2

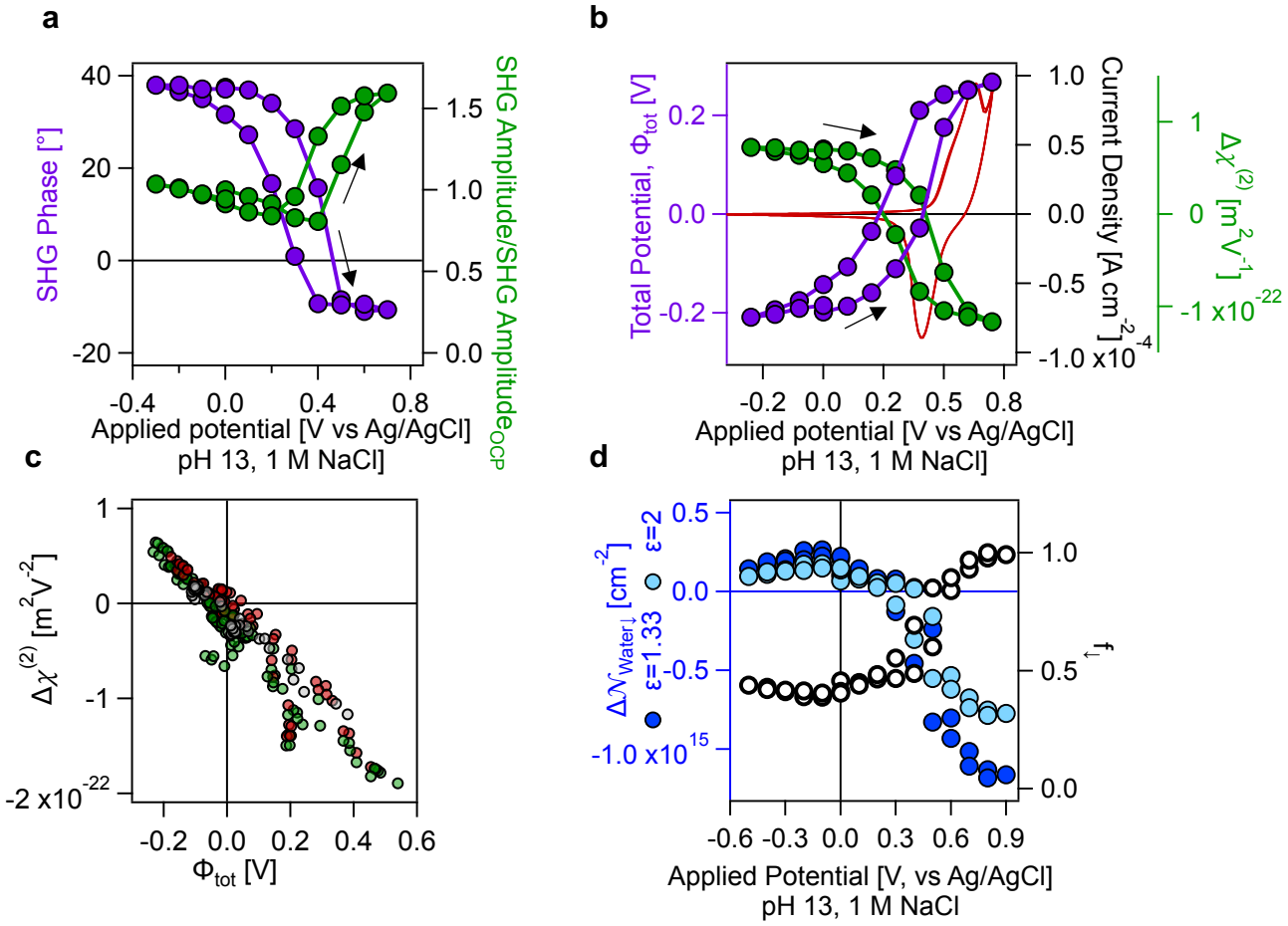
a
SHG Phase [°]
SHG Amplitude/SHG Amplitude$_{OCP}$
Applied potential [V vs Ag/AgCl]
pH 13, 1 M NaCl]
b
Total Potential, Φ_{tot} [V]
Current Density [A cm^{-2}]
$\Delta\chi^{(2)}$ [m^{2}V^{-1}]
Applied potential [V vs Ag/AgCl]
pH 13, 1 M NaCl]
c
$\Delta\chi^{(2)}$ [m^{2}V^{-2}]
Φ_{tot} [V]
d
ΔN_{Water} [cm^{-2}]
ε=2
ε=1.33
$f_{\uparrow}$
Applied Potential [V, vs Ag/AgCl]
pH 13, 1 M NaCl

Fig. 3

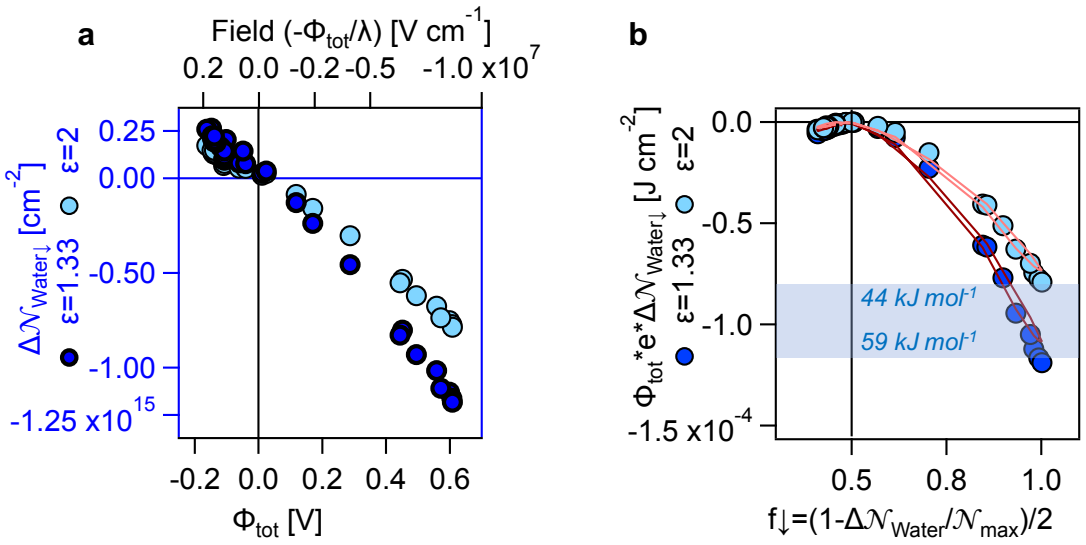
a
Field (-Φtot/λ) [V cm-1]
0.2 0.0 -0.2 -0.5 -1.0 x10^7
ΔNWater↓ [cm-2]
ε=2
ε=1.33
0.25
0.00
-0.50
-1.00
-1.25 x10^15
-0.2 0.0 0.2 0.4 0.6
Φtot [V]
b
Φtot*e*ΔNWater↓ [J cm-2]
0.0
-0.5
-1.0
-1.5 x10^-4
44 kJ mol-1
59 kJ mol-1
0.5 0.8 1.0
f↓=(1-ΔNWater/Nmax)/2